Volume 18, Number 5, 2025. pp. 643-658

Jordan Journal of Physics

ARTICLE

Hadron Therapy with Nanoparticles for Dose Enhancement and Estimation of DNA Damage Using GEANT4

Fatemeh Habibi[a], **Zohreh Parang**[a], **S N Hosseinimotlagh**[a] and **Alireza Keshavarz**[b]

[a] *Department of Physics, Shi.C., Islamic Azad University, Shiraz, Iran.*
[b] *Department of Physics, Shiraz University of Technology, Shiraz, Iran.*

Doi: **https://doi.org/10.47011/18.5.7**

Received on: 02/11/2024; *Accepted on: 20/01/2025*

Abstract: Proton therapy is one of the most promising treatments for several types of tumors, such as those of the eye, brain, and breast, as it benefits from a sharp Bragg peak as well as a spread-out Bragg peak (SOBP) in the tumor region. The Bragg peak helps to deliver the maximum dose to the tumor and the minimum dose to the sensitive organs near the tumor. It has been shown that the addition of nanoparticles to the tumor can improve the treatment gain in radiation therapy. In this study, the microscopic dose enhancement ratio as well as the DNA damage frequency caused by 62.8 MeV protons with the presence of 3000 ppm (i.e., 30 mg/g) Au, Pt, C, ^{11}B, and Fe_3O_4 nanoparticles were investigated using the Geant4-DNA Monte Carlo toolkit. In addition, the cell survival curves were obtained and compared for the condition with and without nanoparticles. All simulations were performed at different locations along the proton range: at the beginning, in the middle, and at the end of the SOBP. The highest dose enhancement in the fibroblast cell was observed for Pt nanoparticles (up to 4%), followed by Au nanoparticles (up to 2.4%), while the lowest dose enhancement was observed for C nanoparticles (up to 0.32%). At the end of the proton range, higher levels of DNA damage were observed than at the beginning of the path and at the center of the SOBP. Unlike some previous studies, this work simulated more realistic clinical conditions, and the obtained results are in good agreement with some experimental results reported in the literature. In conclusion, the combination of Au and Pt nanoparticles with proton therapy has a superiority over C, ^{11}B, and Fe_3O_4 nanoparticles.

Keywords: Hadron therapy, Dose, Nanoparticles, DNA damage, Geant4-DNA.

1. Introduction

Proton therapy is used to treat some common cancerous tumors (such as those of the eye, brain, and lung) with promising clinical outcomes, although it is not yet widespread worldwide [1]. Proton is an interesting radiation source for cancer treatment. At the beginning of its path, a proton leaves relatively low energy in a human phantom, while they deposit the highest amount of energy at the end of its range. This results in the Bragg peak, which is obtained at the end of the proton range when the deposited dose is plotted versus range [2]. The consequence is the delivery of a maximum dose to the tumor with good sparing of sensitive organs and tissues near the tumor. This advantage is not present in conventional X-ray and gamma radiation therapy. It has been shown that gold nanoparticles (Au NPs) can be used to increase the tumor dose in radiation therapy [3-5]. In an in vitro study, Smith et al. [6] showed that the Au NP dose enhancement resulting from a spread-out Bragg peak (SOBP) of 150 MeV protons is less than 5%, which is within experimental uncertainties. Sisin *et al*. [7] measured an Au NP dose enhancement of about 9% (±3%) for 150 MeV proton irradiation using EBT3 radiochromic films. Studies have also been conducted in the field of radiobiology for

Corresponding Author: S N Hosseinimotlagh **Email**: nasrinhosseini_motlagh@iau.ir

proton therapy, one of whose goals is to calculate the relative biological effectiveness (RBE) for protons with different linear energy transfer (LET). Another goal of such studies is to calculate the number and spatial distribution of DNA double-strand breaks (DSBs) caused by protons and then to model cell repair mechanisms and obtain cell survival curves. In general, it has been demonstrated that, from a radiobiological standpoint, proton therapy is more effective in the presence of Au NPs in the tumor [8-14]. Considering laboratory limitations and the lack of easy access to proton therapy facilities, Monte Carlo (MC) simulations have greatly assisted researchers and physicists in dosimetry calculations and treatment planning. Numerous simulation studies have been conducted on Au NP dose enhancement in proton therapy. Some studies have been performed at a macroscopic scale (i.e., the tumor scale), while others have focused on a microscopic scale (i.e., the cellular and DNA scales) [15-21]. Heuskin *et al*. [22] showed that low-energy protons, on the order of 1.3 MeV, can generate up to 32% more secondary electrons around a single Au NP than in the absence of the Au NP. However, they did not report a significant dose enhancement for a mammalian cell model containing a large number of Au NPs. Furthermore, some studies have investigated the effects of Au NP size and distribution on the dose enhancement factor (DEF) in proton therapy [18, 23]. An important point is that, more recently, nanoparticles other than Au, such as superparamagnetic iron oxide (Fe_3O_4),^{11}B, C, Pt, Ag, and Bi NPs, have been investigated for proton therapy [24-28]. Although many interesting simulation studies have been carried out so far, there is an evident discrepancy among some results, which can be attributed to differences in the definition and distribution of Au NPs. In addition, the definition of the proton beam is also important and varies among the relevant studies. In many articles, the proton beam is defined without an accelerator as a monoenergetic radiation source, which differs from the clinical situation, where an SOBP is used to cover the entire tumor. For MC simulations at the microscopic scale, the radiation source has been defined either in the conventional manner (i.e., primary protons) or as a phase space (PS), representing the emission of secondary particles at specific points along the proton range, particularly at the Bragg peak location. One of the problems in some previous simulation studies was that they limited the transport of primary protons to a single NP, such that the incident protons were emitted from the inner surface of an NP and terminated at the opposite surface. This type of source definition appears to suffer from a lack of charged particle equilibrium. A more appropriate approach is to simulate a cell nucleus and consider nanoparticles in large numbers, which has the advantage of allowing the use of a specific mass concentration for nanoparticles (in mg/g or ppm).

Multiscale MC simulations (i.e., simulations at both macroscopic and microscopic scales) have attracted considerable interest in numerous studies [29-34]. Since there is a lack of data in the literature comparing these different simulation models, the present study aims to calculate the microscopic DEF for a therapeutic SOBP proton beam (62.8 MeV) using a multiscale MC simulation. The 62.8 MeV proton beam was chosen because it is a common therapeutic energy for the treatment of ocular tumors [35]. At the macroscopic stage, a phase space (PS) was defined in the middle of the SOBP, and information on the generated secondary particles, along with the primary protons, was stored. These particles were then used as the primary radiation source at the microscopic stage. At the microscopic stage, after defining a mammalian fibroblast cell, various nanoparticles (Au, Pt, C, ^{11}B, and Fe_3O_4) with a concentration of 30 mg/g were randomly implanted in the cytoplasm of the cell [17]. In addition to calculating the DEF induced by nanoparticles in proton therapy, the resulting DNA damage was calculated and compared for the different nanoparticles. Since cancer cell death is ultimately related to radiation-induced DNA damage, cell survival curves were plotted for SOBP irradiation with and without the presence of Au, Pt, C, ^{11}B, and Fe_3O_4 nanoparticles, using a mathematical model of survival and repair implemented in the Geant4-DNA code.

2. Material and Methods

2.1. Simulation Code, Physics, and Chemistry

In this study, the Geant4.11.1.3 MC simulation toolkit [36] with the QGSP_BIC reference physics list was used to obtain the PS

file in a large water phantom. The QGSP_BIC reference physics list has been introduced as an appropriate physics list for proton and hadron therapy simulations [37, 38]. It includes hadronic physics for elastic and inelastic nuclear interactions (i.e., the G4HadronElasticPhysics and G4HadronPhysicsQGSP_BIC classes), electromagnetic standard physics (i.e., the G4EmStandardPhysics class), decay physics (i.e., the G4DecayPhysics class), and other physics related to ions, neutrons, etc. (i.e., the G4EmExtraPhysics, G4StoppingPhysics, G4IonElasticPhysics, G4IonPhysics, and G4NeutronTrackingCut classes). For details on reference physics lists, see [39].

The Geant4-DNA extension [40] was used for the cell-scale simulation for microscopic DEF calculations. It is based on a track-structure algorithm and provides a high accuracy in macroscopic scale simulations. The Geant4-DNA extension includes physics data for the interactions of electrons up to 1 MeV and protons up to 300 MeV energy in liquid water [41-43]. We used the G4EmDNAPhysics_option4 class, which is a recommended class for DNA damage calculations. A detailed overview of the physics models implemented in the Geant4-DNA code for different particles and energy ranges can be found in Refs. [42, 44, 45]. The range cut for the production of secondary particles was set to 1 μm in the phantom (i.e., at the macroscopic stage) and 0.001 μm in the cell (i.e., at the microscopic stage). One of the advantages of the Geant4-DNA code is its capability to model the production, diffusion, and interaction of chemical species (i.e., free radicals) following water radiolysis [46, 47]. In this study, the updated "G4EmDNAChemistry_option3" chemistry constructor, embedded in version 11.1 of the Geant4-DNA code, was used to simulate the pre-chemical and chemical stages. This constructor is based on the synchronous Independent Reaction Times algorithm and includes the most common free radicals, along with their chemical interactions, reaction radii, and reaction rates [48]. For more details on the Independent Reaction Times algorithm, the reader is referred to [48-50]. This capability was used to calculate the indirect DNA damage caused by hydroxyl radicals following water radiolysis, resulting from proton interactions both with and without the presence of various nanoparticles in the cell. The simulation time for the chemical stage was set to 2.5 ns, following the study of Meylan *et al.* [51].

2.2. Cell Modelling and NPs

The cell geometry was defined using the *molecularDNA* example [52] of the Geant4 Monte Carlo toolkit. This model is based on the Hilbert curve, which is a continuous fractal space-filling curve [53]. The fractal geometry is constructed such that a small segment of DNA is continuously repeated in three dimensions in a specific arrangement without overlap. The full DNA chain consists of three types of base voxels: straight, turned, and turned with a 90° twist, and includes histone proteins. The smallest unit of DNA is a base pair (bp), also referred to as a nucleotide pair. Six spheres were modeled as DNA molecules and assembled to construct a nucleotide pair: two bases, two phosphates, and two sugars. Each nucleotide consists of three volumes: 2-deoxyribose, phosphoric acid, and a base, namely adenine ($C_5H_5N_5$), thymine ($C_5H_6N_2O_2$), cytosine ($C_4H_5N_3O$), or guanine ($C_5H_5N_5O$). The histone protein was modeled as a cylinder with a radius of 3.75 nm and a height of 5.75 nm. A histone surrounded by a 216 bp-long DNA helical segment forms a nucleosome. The continuous DNA chain has a total length of 6.4GbP. An ellipsoidal mask was created to confine the DNA chain within an ellipsoidal volume with dimensions of 14.2 × 5.0 × 14.2 μm^3. The effective nucleus density is approximately 0.015 bp per nm^3. Detailed descriptions of the geometrical levels are provided in the relevant publications [54-55]. The nucleus cell geometry is illustrated in Fig. 1. The DNA molecules are not shown in Fig. 1, and the scale of the histones is larger than the actual scale. For visualization purposes, a small number of histones are displayed in Fig. 1. Moreover, eight base boxes with a side length of 75 nm, including straight, turned, and turned-twisted sections, as well as a zoomed-in view of a single histone, are illustrated in Fig. 1.

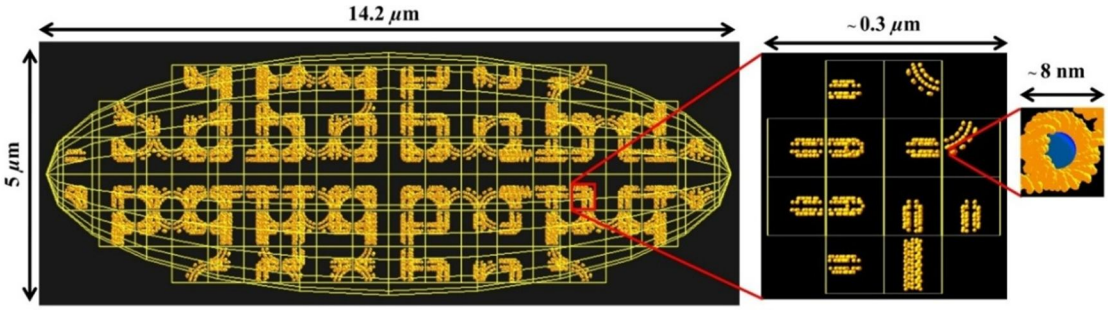

FIG. 1. The nucleus cell geometry taken from the "molecular DNA" example of the Geant4 toolkit.

To define NPs in the cell, an ellipsoid shell of water with a thickness of 1 μm was defined as the cytoplasm around the cell nucleus. So, the whole cell dimensions were 15.2 × 6.0 × 15.2 μm^3 (See Fig. 3). Au, Pt, C, ^{11}B, and Fe_3O_4 NPs, with a radius of 25 nm and a concentration of 30 mg/g (i.e., 3% weight percentage), were randomly distributed in the cytoplasm. Due to the different densities of NP's materials, the number of NPs required for the concentration of 30 mg/g was 17239, 15547, 151227, 144652, and 64352 for Au, Pt, C, ^{11}B, and Fe_3O_4 NPs, respectively.

2.3. Radiation Source

To generate the SOBP and obtain a PS in that region, we used the advanced example "Hadron therapy" [37, 56] of the Geant4 toolkit. This example provides the simulation of several proton and carbon accelerators according to some famous accelerator systems in the world [56-58]. We used the 62.8 MeV proton passive transport beam line in line installed at Laboratori Nazionali del Sud (INFN) in Catania, Italy, which is used for the treatment of eye tumors [56].

In this study, a cube of liquid water with a density of 1 g/cm^3 with dimensions of 25 × 25 × 25 cm^3 was defined as a phantom in front of the proton accelerator. Protons with an energy of 62.8 MeV were then emitted towards the phantom as a beam (with a radius of 2 mm) through the accelerator system. By implementing the default weight factors according to the thickness of the proton range shifter, a~10 mm SOBP was produced using a range modulator wheel and 12 Bragg peaks as 12 initial steps. These default weight factors and the corresponding range shifter thicknesses in the "Hadron therapy" example are listed in Table 1. Details on the design of an SOBP using a range modulator wheel can be found in [35]. Figure 2 shows the SOBP obtained using "Hadron therapy" example with a 62.8 MeV proton beam in a passive transport beam line. The PS was obtained at three locations along the SOBP by defining three virtual detectors with dimensions of 25 × 25 × 0.1 cm³ at the beginning (0.5 mm), middle (26.5 mm), and end (31.5 mm depth) of the SOBP. Information on the primary and secondary particles reaching each detector was recorded and stored in a text file as a PS. The data in each PS file were subsequently used as the primary radiation source for irradiating the fibroblast cell model (see Figure 3). At the cellular scale, the radiation source was defined as a circular planar source with a radius of 7.6 μm to fully cover the cell nucleus and cytoplasm.

TABLE 1. Default weight factors and corresponding range shifter thicknesses used to produce a SOBP from a 62.8 MeV proton beam in the "Hadron therapy" example of the Geant4 Monte Carlo toolkit.

Step Numbers	Step Thickness (mm)	Relative Wight factor
1	0.0	0.28215
2	0.84	0.06864
3	1.68	0.09704
4	2.52	0.05974
5	3.36	0.07385
6	4.20	0.05965
7	5.04	0.06518
8	5.88	0.05708
9	6.72	0.06055
10	7.56	0.05762
11	8.40	0.05942
12	9.24	0.05908

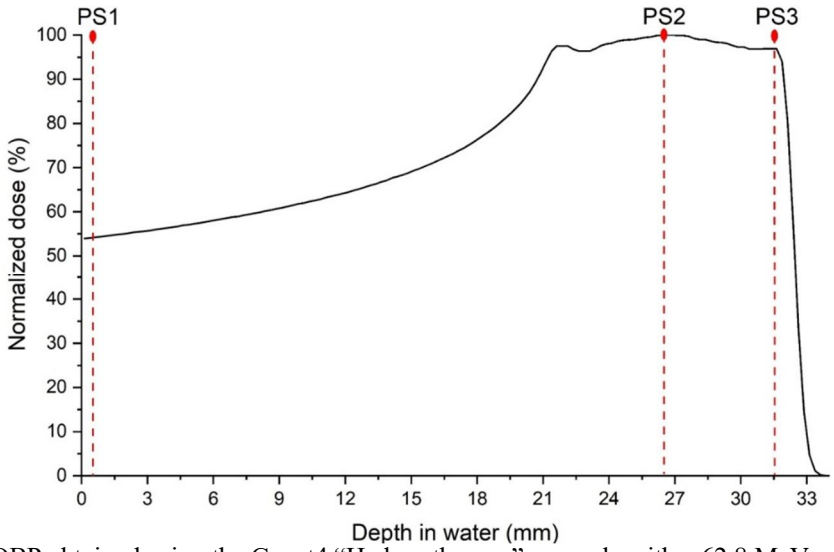

FIG. 2. The SOBP obtained using the Geant4 "Hadron therapy" example with a 62.8 MeV proton beam in a passive transport beam line. The locations of obtaining the phase-space (PS) are indicated by three dashed lines at depths of 0.5 mm (at the beginning), 26.5 mm (at the middle), and 31.5 mm (at the end).

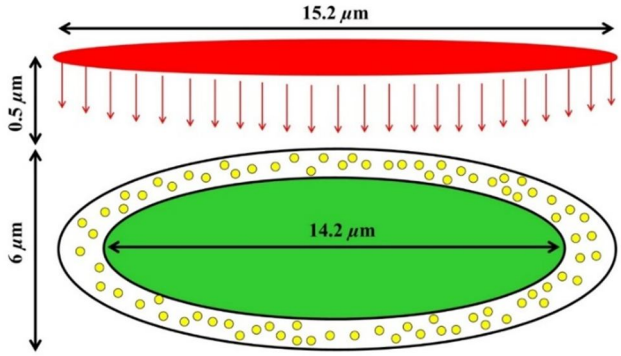

FIG. 3. The cell model irradiated by a circular plane source with a radius of 7.6 μm, emitting particles from a phase-space file.

2.4. DEF and DNA Damage Calculation

If D_{NP} and D_0 are the doses deposited in the cell with and without NPs in its cytoplasm, respectively, the DEF is calculated using Eq. (1):

$$DEF = D_{NP}/D_0 \quad (1)$$

According to the study of Nikjoo *et al*. [59], DNA damage has two general categories: single- and double-strand breaks (SSBs and DSBs). DNA damage can also be classified as direct (caused by the radiation), indirect (caused by free radicals), or hybrid. Figure 4 displays the classification of DNA damage that is the result of physical and chemical stages [60]. Two types of complex DSBs, i.e., DSB+ and DSB++, are also shown in Fig. 4. These complex lesions are essential for a mathematical model of cell repair and survival.

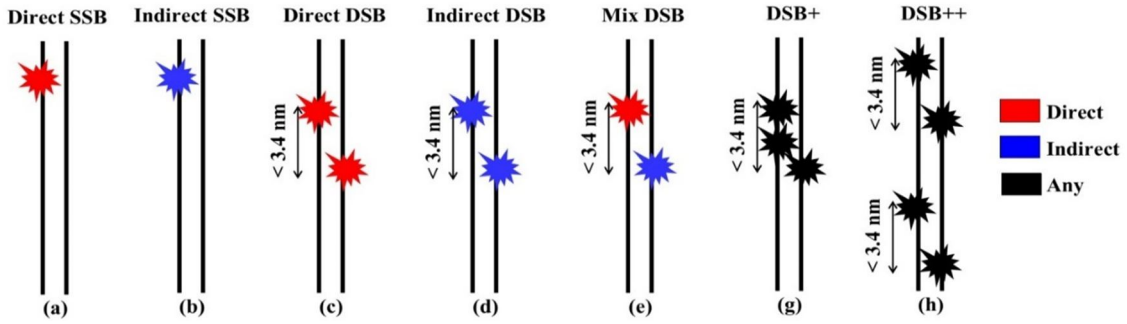

FIG. 4. Categorization of DNA damage: (a) direct and (b) indirect single-strand break (SSB); (c) direct and (b) indirect, and (c) mixed double-strand break (DSB). Two types of complex DSBs are also shown as DSB+ and DSB++.

SSB may be recorded when an energy deposition of 5 eV or greater occurs in the backbone of the DNA (i.e., sugar-phosphate volumes). It is the minimum energy threshold for the SSB occurrence, and the probability of SSB occurrence increases linearly with the deposited energy. The maximum energy threshold for the SSB occurrence is 37.5 eV, which means the probability of an SSB will be 100% when an energy deposition of 37.5 eV or greater occurs in the backbone of the DNA [61]. Two SSBs located on opposite DNA strands with a distance of less than ~3.4 nm (or 10 bps) lead to a DSB. To consider the quasi-direct effect, a radial distance of 0.6 nm beyond each sugar-phosphate molecule was determined as the hydration shell. This effect refers to the damage caused by charge transfers following ionization of the hydration shell around the DNA molecules [62]. In the case of indirect DNA damage, the presence of the chemical species in the sugar-phosphate molecules may lead to SSB. Only the hydroxyl radical ($OH^{\bullet}$) was taken into account for calculating indirect DNA damage, since it is the most reactive radical. Furthermore, only a proportion of $OH^{\bullet}$ radicals lead to indirect SSB. A probability of 40% was set for each $OH^{\bullet}$ radical reaching to the sugar-phosphate molecule to result in an indirect SSB [52, 54, 63]. Note that all chemical species that diffuse more than 4 nm from the DNA molecules were killed, as their effective diffusion range is roughly 4 nm for DNA damage calculation [59]. An 80 CPU-core computing system with 180 GB of RAM was used for this study. A statistical error of less than 1% was obtained for dose calculation with 2, 1, and 0.5 million initial particles for PS1, PS2, and PS3 files, respectively.

2.5. Cell Survival Calculation

The DNA damage yields induced by ionizing radiation increase during irradiation. A proportion of DNA damages are repaired over time. The freely available Python codes provided in the "molecularDNA" example of the Geant4 toolkit were used to obtain the cell survival fraction. Two mathematical models have been integrated with the Geant4-DNA code to estimate the cell survival fraction [64, 65]: the Two-Lesion Kinetic (TLK) model [66] and the Local Effect model (LEM) [67]. In this study, the TLK model was employed to estimate the cell survival fraction. The TLK model establishes a link between double-strand breaks (DSBs) and cell death, based on the complexity of DNA damage. It assumes that DSB repair depends on the complexity of the damage, with DSB+ and DSB++ considered as complex and lethal DNA lesions. The TLK model incorporates both slow and fast DNA repair mechanisms, which account for first-order (single-lesion) and second-order (multiple-lesion) repair processes. The first- and second-order repairs are represented by the parameters L(t) and $L^2(t)$, respectively, at time t after the irradiation. These repair mechanisms consider both the correct rejoining of the free ends of damaged DNA base pairs at their original locations and the incorrect rejoining at different positions. The second-order repair can therefore lead to fatal chromosomal aberrations. The TLK model calculates the cell survival fraction using the following equations [66]:

$$\frac{dL_1(t)}{dt} = \dot{D}(t)Y\Sigma_1 - \lambda_1 L_1(t) - \eta L_1[L_1(t) + L_2(t)] \quad (2)$$

$$\frac{dL_2(t)}{dt} = \dot{D}(t)Y\Sigma_2 - \lambda_2 L_2(t) - \eta L_2[L_1(t) + L_2(t)] \quad (3)$$

$$\frac{dL_f(t)}{dt} = \beta_1\lambda_1 L_1(t) + \beta_2\lambda_2 L_2(t) + \gamma\eta[L_1(t) + L_2(t)]^2 \quad (4)$$

Here, $L_1(t)$ and $L_2(t)$ are the frequencies of simple DSBs (fast repair) and complex DSBs (slow repair), respectively, per irradiated cell at time t. $L_f(t)$ represents the number of lethal DNA damages that may lead to cell death. Y is the genome length in Gbps, and $\dot{D}(t)$ is the dose rate. Σ_1 and Σ_2 are the frequencies of simple and complex DSBs, respectively. Simple (Σ_1) DSBs are equal to the number of isolated DSBs, i.e., DSBs other than DSB+ and DSB++. Complex (Σ_2) DSBs are considered to be $N_{DSB+} + 2N_{DSB++}$ [52, 64]. Simple and complex DNA damages are repaired by fast and slow repair processes, respectively. η and λ are repair probability factors that describe the rate of damage rejoining (h^{-1}). β and γ are the lethality probability factors that describe the likelihood that residual damage may lead to cell death. The subscripts 1 and 2 for λ and β parameters correspond to simple and complex lesions, respectively. All parameters were set for a fibroblast cell nucleus according to Chatzipapas *et al.* [52]. The cell survival fraction was then calculated by Eq. (5):

$$\text{Survival Fraction} = e^{-L_f} \quad (5)$$

Figure 5 shows the time variations of (a) $L_1(t)$, (b) $L_2(t)$, (c) $L_f(t)$, and (d) the survival fraction, calculated using Eqs. (2)-(5) with the fourth-order Runge-Kutta method.

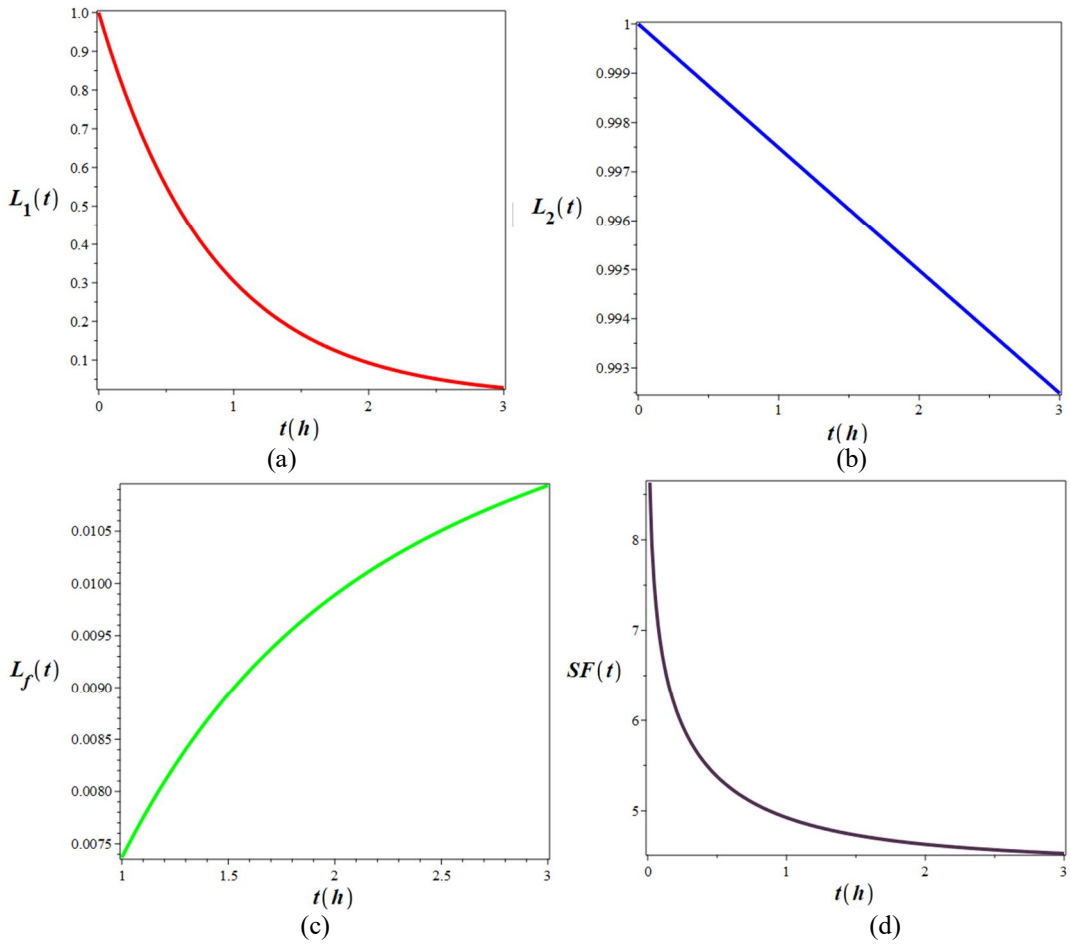

FIG. 5. Time variations of (a) $L_1(t)$, (b) $L_2(t)$, (c) $L_f(t)$, and (d) survival fraction.

The fraction of activity released (FAR), measured using gel-electrophoresis methods, is used to quantify the number and size of DNA fragments resulting from DNA fiber breakage, such as that induced by DSBs. By calculating the ratio between FAR and the initial FAR, it is possible to estimate the fraction of un-rejoined DSBs. According to the random-breakage model, the relationship between FAR and the number of un-rejoined DSBs ($(L_1(t) + L_2(t))/Y$) can be calculated using the following equation:

$$FRA(t) = F_{max}\{1 - [1 + K(L_1(t) + L_2(t))/Y(1 - \frac{K}{M_0})]\exp(-K(L_1(t) + L_2(t))/Y)\} \quad (6)$$

In Fig. 6, we plotted the time variations of $FRA(t)$ using Eq. (6).

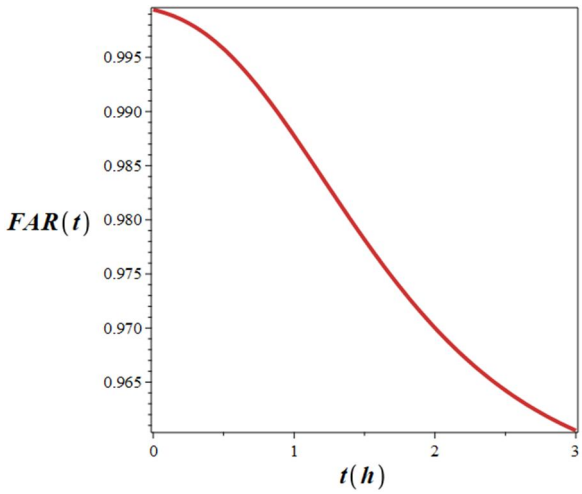

FIG. 6. Time variations of $FRA(t)$.

3. Results

For validating the simulation, the Bragg peak curve of 62.8 MeV protons in water obtained using Geant4 in this study was compared with experimental data (obtained with an ion chamber) provided by the example "Hadron therapy" [37, 56]. As can be seen in Fig. 7, good agreement is obtained between the simulation and the reference data.

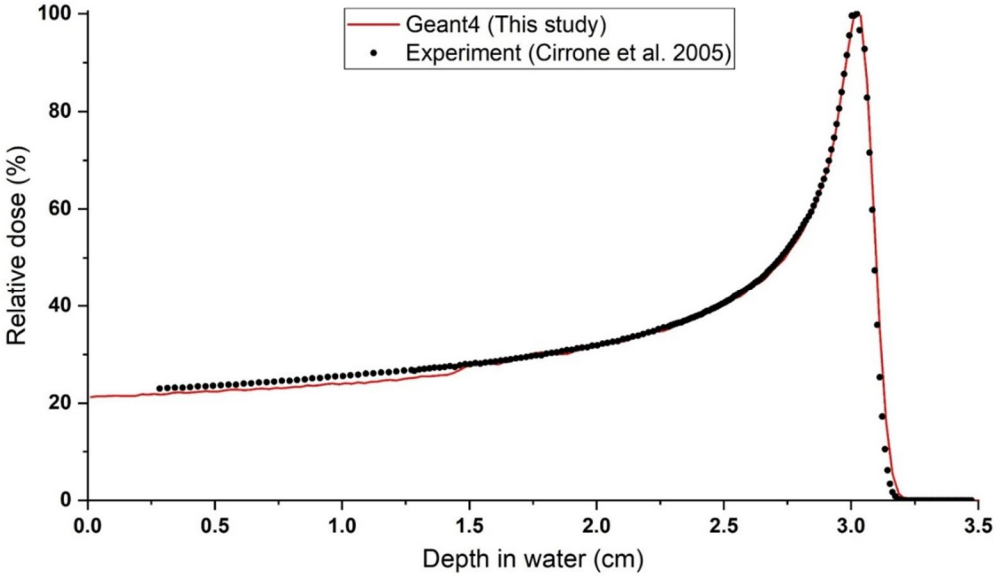

FIG. 7. Comparison of Bragg peak curves obtained using the Geant4 toolkit and experimental data obtained with an ion chamber [37, 56].

Figure 8 shows the DEF (%) for Au, Pt, C, ^{11}B, and Fe_3O_4 NPs at a concentration of 30 mg/g distributed in the cytoplasm of the cell. Figure 9 shows the DNA damage enhancement (SSBs and DSBs) caused by the presence of 30 mg/g Au, Pt, C, ^{11}B, and Fe_3O_4 NPs in the cell cytoplasm. The ratio of direct to indirect total DNA damages (D_{dir}/D_{ind}) and the ratio of DSB/SSB for 30 mg/g Au, Pt, C, ^{11}B, and Fe_3O_4 NPs in the cell cytoplasm are listed in Table 2. The ratios are presented for three PSs shown in Fig. 2.

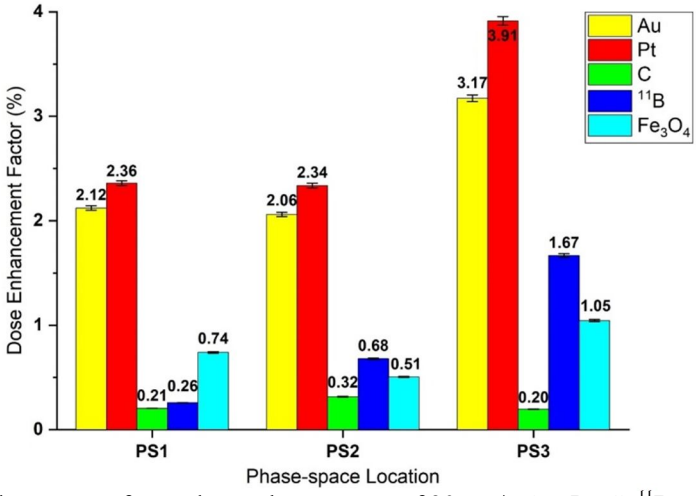

FIG. 8. The dose enhancement factor due to the presence of 30 mg/g Au, Pt, C, ^{11}B, and Fe_3O_4 NPs in the cytoplasm of the cell.

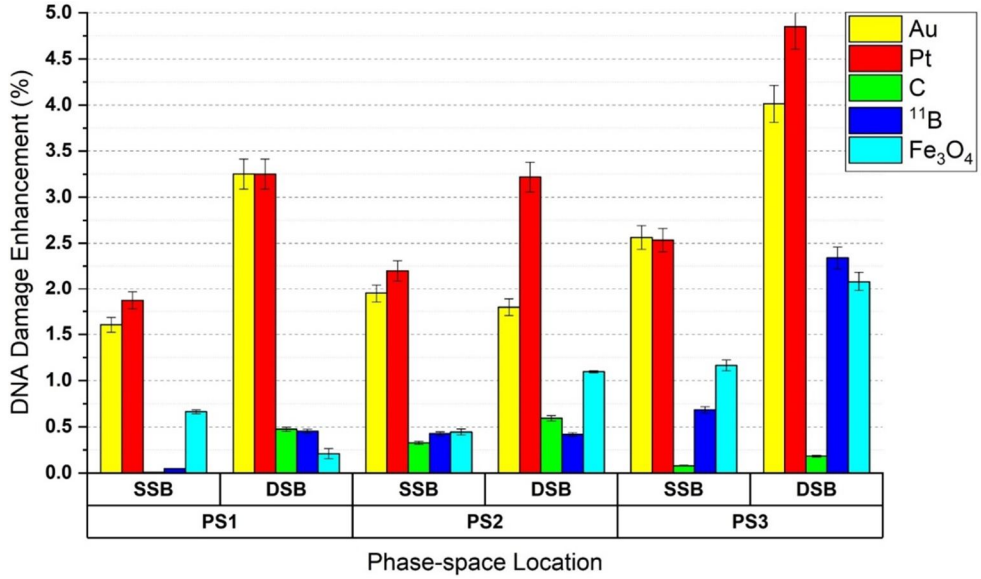

FIG. 9. Enhancement in the single- and double-strand DNA breaks (SSBs and DSBs) due to the presence of 30 mg/g Au, Pt, C, ^{11}B, and Fe_3O_4 NPs in the cytoplasm of the cell.

TABLE 3. Ratios of single- to double-strand breaks (DSB/SSB) and direct- to indirect-DNA damage (D_{dir}/D_{ind}) for various NPs in the cell irradiated by particles in three phase-spaces.

NP material	D_{dir}/D_{ind}			DSB/SSB		
	PS1	PS2	PS3	PS1	PS2	PS3
Au	1.346	1.491	1.655	0.0667	0.0833	0.1132
Pt	1.349	1.484	1.652	0.0665	0.0842	0.1169
C	1.341	1.485	1.649	0.0660	0.0836	0.1116
^{11}B	1.340	1.488	1.656	0.0659	0.0834	0.1135
Fe_3O_4	1.341	1.487	1.649	0.0661	0.0830	0.1127

The numbers of repairable and irreparable DSBs per primary particle induced in the cell nucleus, with and without the presence of 30 mg/g Au, Pt, C, ^{11}B, and Fe_3O_4 NPs are listed in Table 3. Figure 10 shows a comparison of the cell survival curves obtained from the TLK model with and without 30 mg/g Pt nanoparticles in the cell cytoplasm. The error bars are small and fall within the marker size. According to Table 3, Pt nanoparticles produced the highest DNA damage among the tested NPs; therefore, only the cell survival curves for Pt are shown.

TABLE 3. The frequency of repairable and irreparable DSBs per primary particle induced in the cell nucleus with and without different NPs (30 mg/g).

NP material (30 mg/g)	PS1 (0.5 mm)		PS2 (26.5 mm)		PS3 (31.5 mm)	
	Repairable DSBs/event	Irreparable DSBs/event	Repairable DSBs/event	Irreparable DSBs/event	Repairable DSBs/event	Irreparable DSBs/event
H_2O (No NP)	0.09041	0.04085	0.13415	0.06905	0.16982	0.09893
Au	0.09316	0.04215	0.13594	0.07134	0.17598	0.10439
Pt	0.09294	0.04250	0.13824	0.07179	0.18324	0.11218
C	0.09049	0.04143	0.13459	0.07001	0.17015	0.10029
^{11}B	0.09045	0.04153	0.13472	0.06921	0.17332	0.10273
Fe_3O_4	0.09109	0.04165	0.13419	0.06934	0.17339	0.10155

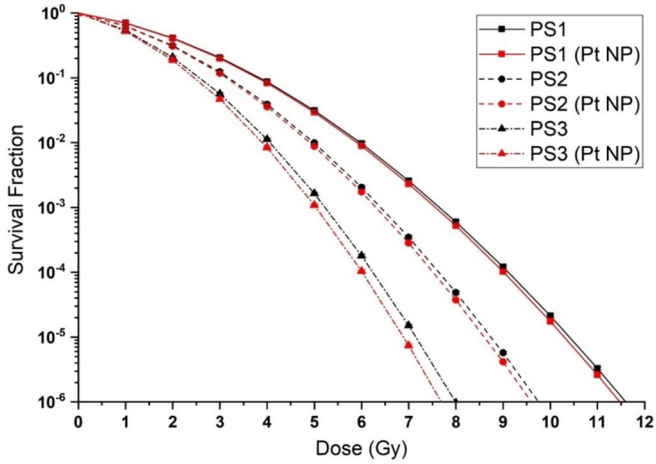

FIG. 10. Cell survival curves obtained from the TLK model with and without 30 mg/g Au, Pt, C, ^{11}B, and Fe_3O_4 NPs in the cell cytoplasm.

Figures 11 and 12 show the numerical values of the calculated dose and DEF, respectively, for selected NPs in terms of proton beam energy at the phantom cell.

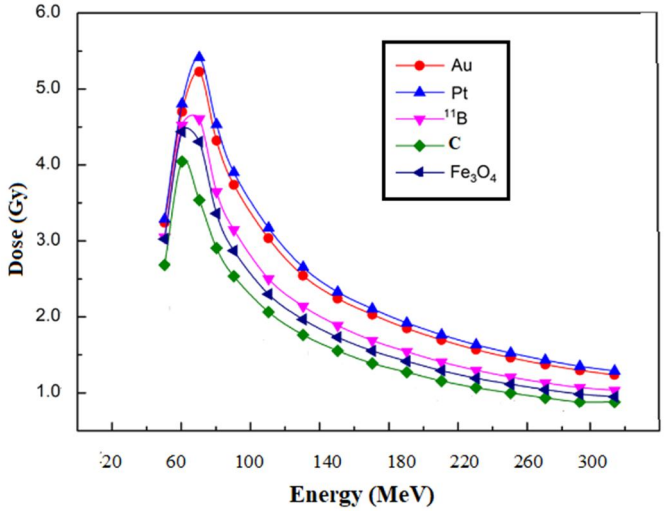

FIG. 11. Calculated dose for five different nanoparticles as a function of proton beam energy at the cell phantom.

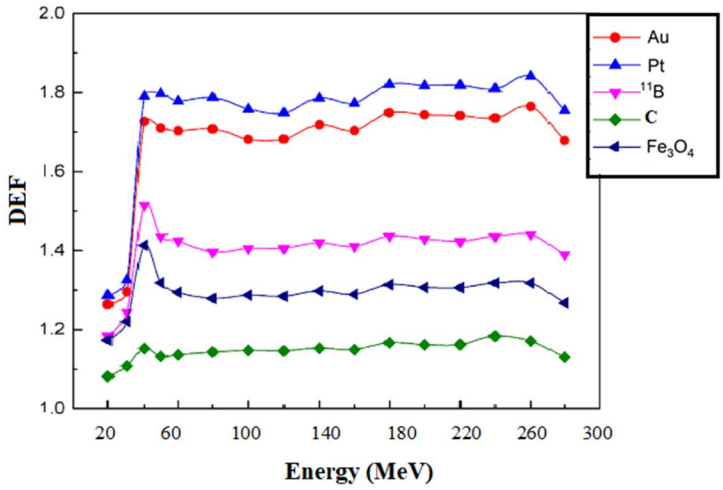

FIG. 12. Calculated DEF values for five different nanoparticles as a function of proton beam energy in the phantom.

Figure 13 presents a three-dimensional plot to show the dependency of DEF on the size and concentration of distributed NPs in the phantom irradiated with 62.5 MeV protons.

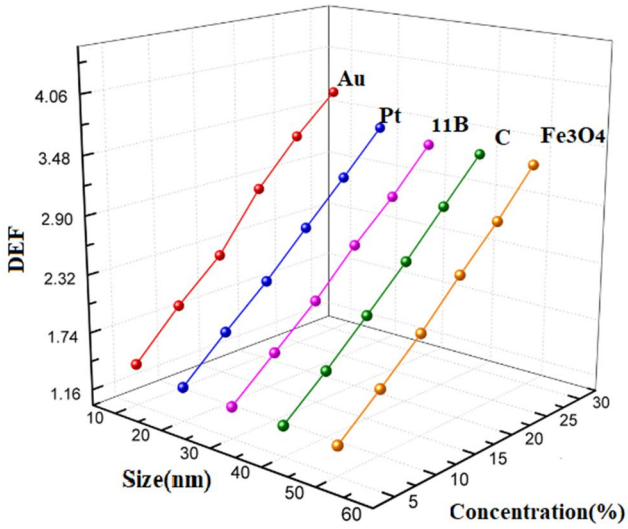

FIG. 13. Three-dimensional variations of DEF in terms of the size and concentration of selected NPs distributed in the phantom.

4. Discussion

Figure 6 shows that Pt NPs have the highest DEF in the cell nucleus among the studied NPs. At the beginning and middle of the proton range (i.e., for PS1 and PS2, respectively), the DEF difference between Pt and Au NPs is up to 13.5%, while at the end of the SOBP (i.e., for PS3), this difference reaches about 23.3%. For all PSs, Pt and Au NPs showed significant differences in DEF compared to other studied NPs. After Pt and Au, ^{11}B NPs seem to show a better effect. At the end of the range, ^{11}B NPs showed an increase of 101% and 427% in the DEF relative to the beginning and center of the SOBP, respectively. At that location, Fe_3O_4 NPs showed an increase of 41.9% and 106% in the DEF compared to the beginning and center of the SOBP, respectively. Among the studied NPs, C NPs had the lowest DEF in the cell. C and B elements have close atomic numbers and almost similar density (about 2.3 g/cm^3 at standard conditions) and can both produce alpha particles via nuclear interactions with protons [26, 68]:

$$p + {}^{12}C \rightarrow 3\alpha + p \quad (7)$$

$$p + {}^{11}B \rightarrow 3\alpha \quad (8)$$

Nevertheless, the observed differences in DEF arise from the cross sections of these nuclear interactions. The probability of such reactions is very low; for example, in the proton energy range of 50–60 MeV, the reaction cross section with carbon is only 400 mb (i.e., 10^{-27} cm^2). This means that the majority of transported particles are primary protons, secondary electrons, and photons, whereas alpha particles have a very small contribution in dose calculations. For 5×10^5 incident protons, only 3 alpha particles were recorded in the PS at the Bragg peak, i.e., only a single interaction occurred. In the case of PS1 and PS2 locations, there were zero alpha particles in the PS file for 2×10^6 and 10^6 incident protons, respectively. However, if we consider only certain nuclear interactions or only secondary particles, the DEF results will be completely different, but this does not correspond to the real conditions. The fact that by approaching the end of the SOBP, the effectiveness of ^{11}B NPs becomes higher than the previous positions is consistent with the results of Cirrone *et al*. [68] and Beni et al. [69]. The reason is that the cross-section of the above-mentioned interactions is greater at the Bragg peak, i.e., in the energy range of 0.1-10 MeV.

Although previous studies reported a large dose increase with C nanoparticles, the discrepancy with our results arises from differences in simulation methodology [20, 21, 25, 70]. In those studies, a single NP was simulated, and all primary particles directly hit that NP. In such cases, the probability of nuclear interactions is much higher, and secondary particles directly enter the target volume, which is considered a uniform water volume without DNA details. Furthermore, some studies assumed mono-energetic incident protons, unlike the realistic SOBP used clinically. These differences in simulation setup are the main reasons for the discrepancies in DEF between our results and previous studies. In this work, we aimed to simulate a more realistic scenario by incorporating the full energy spectrum of protons

in the center of the SOBP a detailed nucleus cell model, and a realistic distribution of nanoparticles at a defined concentration in the cytoplasm. The DEF of approximately 3% with Au nanoparticles obtained in our simulation is in good agreement with experimental data, which report increases of up to 9 % [6,7].

McKinnon *et al*. [70] reported a 27% increase in dose for Au nanoparticles using the Geant4 toolkit. In that study, as in many other simulation studies, only a single NP was considered, and all primary particles directly hit that NP, with the dose calculated in ring detectors up to a radius of 2 μm from the NP center. Other studies using the same single-NP approach reported DEF values of up to 1600% for Au and Pt nanoparticles [20, 21]. However, experimental studies indicate that such dose increases are inconsistent with real conditions, a finding confirmed by our simulation study.

Our results are consistent with the simulation study of Sotiropoulos *et al*. [17], which considered a whole-cell model with Au nanoparticles in the cytoplasm. However, they did not observe a significant increase in direct DNA damage for a concentration of 7 mg/g Au NPs when irradiating cells with 10 and 50 MeV protons. In contrast, as shown in Fig. 7, the present study demonstrates a 24% increase in DNA damage across different PS files. This difference arises because Sotiropoulos *et al*. [17] considered only direct DNA damages, whereas we accounted for both direct and indirect damages, highlighting the importance of including indirect damages resulting from water radiolysis.

The higher DEF of Pt nanoparticles compared to Au nanoparticles at the center of the SOBP, as well as at the other two PS locations (Fig. 6), is in good agreement with experimental results reported in the literature [71-73].

This superiority of Pt NPs over Au NPs, for the same size and concentration, is attributed to the physicochemical properties of Pt that enhance the production of chemical species following irradiation [73]. As the end of the SOBP is approached, the amount of DNA damage per incident particle increases compared to the previous PS locations, which aligns with other published studies [17,74]. This effect is due to the higher linear energy transfer (LET) at the end of the Bragg peak.

According to Table 3, the observed increase in the D_{dir}/D_{ind} ratio with increasing LET (corresponding to greater depth in water) is consistent with the findings of other studies [75-77]. Furthermore, the enhancement of the DSB/SSB ratio with increasing LET agrees with the results reported by Chattaraj and Selvam [78] and Rafiepour *et al*. [79].

Table 3 shows that as the atomic number of the NPs increases, the normalized DSB damages per event, which include repairable (simple DSBs) and irreparable (complex DSBs) damages, increase. Therefore, the calculated DSBs are higher for Au and Pt NPs, which explains the higher DEF in the cell compared to other NPs. However, this increase is negligible for protons compared to low-energy photons, because low-energy photons have an extremely high cross-section with materials of high atomic number [4, 6, 17]. Needless to say, atomic number is not the only main factor; other factors also play a role in this dose increase. For instance, higher density increases collisions with target molecules, and specific physicochemical properties of the NPs, demonstrated experimentally, can also influence dose enhancement. DSBs are used as input for the TLK mathematical model, the results of which are shown in the cell survival curves in Fig. 8. As illustrated, the cell survival curves with and without Pt NPs show no significant difference at the beginning and middle of the SOBP (two PSs), but the difference is significant at the end of the SOBP. Although the choice of mathematical model and parameter values can strongly affect the final shape of the survival curves, the observed difference between the curves with and without NPs is the key finding in this study. The variation in cell survival curves with different LETs, i.e., at different PS locations, is consistent with other relevant studies [8, 79-81]. Figure 9 presents the calculated dose in the phantom volume resulting from irradiation with monoenergetic protons ranging from 20 to 320 MeV. The dose plot for Pt NPs shows a superior curve compared to other NPs, indicating the greater efficacy of Pt in enhancing dose. The maximum dose for Pt NPs is approximately 5.34 Gy at 60 MeV protons. Figure 10 shows that the calculated DEF values strongly depend on the proton beam energy. The peak positions are similar for all five NPs, with maximum DEF values occurring in the energy range of 30-280 MeV. The results indicate that

Pt NPs outperform other nanoparticles in increasing dose rate, with DEF increasing 1.8 times over this energy range, resulting in a significant dose enhancement.

Therefore, further studies were performed using Pt NPs to investigate different parameters. Although DEF varies linearly with NP concentration, it is relatively insensitive to NP size. For concentrations of 5% and 30%, the DEFs for different NP sizes vary by approximately 8% and 13%, respectively. Based on these results, the size of Pt NPs distributed in the phantom is not a critical factor in predicting or controlling dose and DEF in the tumor volume.

5. Conclusion

A multiscale simulation was performed to study the dose enhancement factor (DEF) resulting from the presence of Au, Pt, C, ^{11}B, and Fe_3O_4 nanoparticles at a concentration of 30 mg/g in a fibroblast cell model under SOBP irradiation with 62.8 MeV protons. The results showed that high atomic number NPs, such as Au and Pt, are promising agents for 62.8 MeV proton therapy, as they can enhance the cell dose by up to 4%. The radiobiological impact of Au and Pt NPs, assessed through cell survival curves, also confirmed this conclusion. Although the results differ significantly from some previous simulation studies, this study highlights the importance of considering realistic clinical conditions. In summary, the Geant4 toolkit was used to perform a comparative study of NP properties and proton beam energy. Nanoparticles of different concentrations and sizes were distributed throughout the selected cell, and the DEF in the nucleus was calculated for various energies and materials. This study concludes that dose enhancement depends both on the incident proton energy and on the type of nanoparticle material.

References

[1] Mohan R., Precis. Radiat. Oncol., 6 (2) (2022) 164.

[2] Newhauser, W.D. and Zhang, R., Phys. Med. Biol., 60 (8) (2015) R155.

[3] Hainfeld, J.F., Dilmanian, F.A., Slatkin, D.N., and Smilowitz, H.M., J. Pharm. Pharmacol., 60 (8) (2008) 977.

[4] Rudek, B., McNamara, A., Ramos-Méndez, J., Byrne, H., Kuncic, Z., and Schuemann, J., Phys. Med. Biol., 64 (17) (2019) 175005.

[5] Cunningham, C., de Kock, M., Engelbrecht, M., Miles, X., Slabbert, J., and Vandevoorde, C., Front. Public Health, 9 (2021) 699822.

[6] Smith, C.L., Best, S.P., Gagliardi, F., Tominaga, T., and Geso, M., Radiat. Meas., 106 (2017) 352.

[7] Sisin, N.N.T. et al., Radiat., 2 (1) (2022) 130.

[8] Polf, J.C., Bronk, L.F., Driessen, W.H., Arap, W., Pasqualini, R., and Gillin, M., Appl. Phys. Lett., 98 (19) (2011) 193702.

[9] Kim, J.K., Seo, S.J., Kim, H.T., Kim, K.H., Chung, M.H., Kim, K.R., and Ye, S.J., Phys. Med. Biol., 57 (24) (2012) 8309.

[10] Hojo, H., Dohmae, T., Hotta, K., Kohno, R., Motegi, A., Yagishita, A., Makinoshima, H., Tsuchihara, K., and Akimoto, T., Radiat. Oncol., 12 (1) (2017) 111.

[11] Li, S., Bouchy, S., Penninckx, S., Marega, R., Fichera, O., Gallez, B., Feron, O., Martinive, P., Heuskin, A.C., Michiels, C., and Lucas, S., Nanomedicine, 14 (3) (2019) 317.

[12] Torrisi, L., Davidkova, M., Havranek, V., Cutroneo, M., and Torrisi, A., Radiat. Eff. Defects Solids, 175 (9-10) (2020) 863.

[13] Lo, C.Y., Tsai, S.W., Niu, H., Chen, F.H., Hwang, H.C., Chao, T.C., Hsiao, I.T., and Liaw, J.W., ACS Omega, 8 (20) (2023) 17922.

[14] Velten, C. and Tomé, W.A., Biomed. Phys. Eng. Express, 9 (4) (2023) 045004.

[15] Martínez-Rovira, I. and Prezado, Y., Med. Phys., 42 (11) (2015) 6703.

[16] McNamara, A.L., Kam, W.W., Scales, N., McMahon, S.J., Bennett, J.W., Byrne, H.L., Schuemann, J., Paganetti, H., Banati, R., and Kuncic, Z., Phys. Med. Biol., 61 (16) (2016) 5993.

[17] Sotiropoulos, M., Taylor, M.J., Henthorn, N.T., Warmenhoven, J.W., Mackay, R.I., Kirkby, K.J., and Merchant, M.J., Biomed. Phys. Eng. Express, 3 (2) (2017) 025025.

[18] Peukert, D., Kempson, I., Douglass, M., and Bezak, E., Med. Phys., 47 (2) (2020) 651.

[19] Huynh, N.H. and Chow, J.C., Appl. Sci., 11 (22) (2021) 10856.

[20] Rajabpour, S., Saberi, H., Rasouli, J., and Jabbari, N., Sci. Rep., 12 (1) (2022) 1779.

[21] Mansouri, E., Almisned, G., Tekin, H.O., Rajabpour, S., and Mesbahi, A., Radiat. Environ. Biophys., 63 (2024) 537.

[22] Heuskin, A.C., Gallez, B., Feron, O., Martinive, P., Michiels, C., and Lucas, S., Med. Phys., 44 (8) (2017) 4299.

[23] Lin, Y., McMahon, S.J., Paganetti, H., and Schuemann, J., Phys. Med. Biol., 60 (10) (2015) 4149.

[24] Ahn, S.H., Lee, N., Choi, C., Shin, S.W., Han, Y., and Park, H.C., Phys. Med. Biol., 63 (11) (2018) 114001.

[25] Tabbakh, F., Hosmane, N.S., Tajudin, S.M., Ghorashi, A.H., and Morshedian, N., Sci. Rep., 12 (1) (2022) 17404.

[26] Tabbakh, F. and Hosmane, N.S., Eur. Phys. J. Plus, 138 (6) (2023) 538.

[27] Zavestovskaya, I.N., Popov, A.L., Kolmanovich, D.D., Tikhonowski, G.V., Pastukhov, A.I., Savinov, M.S., Shakhov, P.V., Babkova, J.S., Popov, A.A., Zelepukin, I.V., Grigoryeva, M.S., Shemyakov, A.E., Klimentov, S.M., Ryabov, V.A., Prasad, P.N., Deyev, S.M., and Kabashin, A.V., Nanomaterials, 13 (15) (2023) 2167.

[28] Zavestovskaya, I.N. et al., Mater. Today, Nano, 27 (2024). 100508.

[29] Lin, Y., McMahon, S.J., Scarpelli, M., Paganetti, H., and Schuemann, J., Phys. Med. Biol., 59 (24) (2014) 7675.

[30] Klapproth, A.P., Schuemann, J., Stangl, S., Xie, T., Li, W.B., and Multhoff, G., Cancer Nanotech., 12 (2021) 27.

[31] Martinov, M.P., Fletcher, E.M., and Thomson, R.M., Med. Phys., 50 (9) (2023) 5853.

[32] Martinov, M.P., Fletcher, E.M., and Thomson, R.M., Med. Phys., 50 (9) (2023) 5842.

[33] Rafiepour P., Sina S., and Mortazavi S.M.J., Radiat. Phys. Chem., 212 (2023) 111016.

[34] Ganjeh, Z.A. and Mosleh-Shirazi, M.A., Radiat. Phys. Chem., 214 (2024) 111289.

[35] Jia, S.B., Romano, F., Cirrone, G.A., Cuttone, G., Hadizadeh, M.H., Mowlavi, A.A., and Raffaele, L., Nucl. Instrum. Methods Phys. Res. A, 806 (2016) 101.

[36] Agostinelli, S. et al., Nucl. Instrum. Methods Phys. Res. A, 506 (2003) 250.

[37] Cirrone, G.P. et al., IEEE Trans. Nucl. Sci., 52 (1) (2005) 262.

[38] Allison, J. et al., Nucl. Instrum. Methods Phys. Res. A, 835 (2016) 186.

[39] Geant4 Collaboration, Guide for Physics Lists (Geant4 version 11.1), (2023).

[40] Incerti, S. et al., Int. J. Model. Simul. Sci. Comput., 01 (02) (2010) 157.

[41] Bernal, M.A. et al., Phys. Med., 31 (8) (2015) 861.

[42] Incerti, S., Kyriakou, I., Bernal, M.A., Bordage, M.C., Francis, Z., Guatelli, S., Ivanchenko, V., Karamitros, M., Lampe, N., Lee, S.B., Meylan, S., Min, C.H., Shin, W.G., Nieminen, P., Sakata, D., Tang, N., Villagrasa, C., Tran, H.N., and Brown, J.M.C., Med. Phys., 45 (8) (2018) e722.

[43] Domínguez-Muñoz, A.D., Gallardo, M.I., Bordage, M.C., Francis, Z., Incerti, S., and Cortés-Giraldo, M.A., Radiat. Phys. Chem., 199 (2022) 110363.

[44] Incerti, S., Ivanchenko, A., Karamitros, M., Mantero, A., Moretto, P., Tran, H.N., Mascialino, B., Champion, C., Ivanchenko, V.N., Bernal, M.A., Francis, Z., Villagrasa, C., Baldacchin, G., Guèye, P., Capra, R., Nieminen, P., and Zacharatou, C., Med. Phys., 37 (9) (2010) 4692.

[45] Kyriakou, I., Sakata, D., Tran, H.N., Perrot, Y., Shin, W.G., Lampe, N., Zein, S., Bordage, M.C., Guatelli, S., Villagrasa, C., Emfietzoglou, D., and Incerti, S., Cancers, 14 (1) (2021) 35.

[46] Karamitros, M., Incerti, S., and Mantero, A., Prog. Nucl. Sci. Technol., 2 (2011) 503.

[47] Karamitros, M. et al., J. Comput. Phys., 274 (2014) 841.

[48] Tran, H.N., Ramos-Méndez, J., Shin, W.G., Perrot, Y., Faddegon, B., Okada, S., Karamitros, M., Davídková, M., Štěpán, V., Incerti, S., and Villagrasa, C., Med. Phys., 48 (2) (2021) 890.

[49] Plante, I. and Devroye, L., Radiat. Phys. Chem., 139 (2017) 157.

[50] Ramos-Méndez, J., Shin, W.G., Karamitros, M., Domínguez-Kondo, J., Tran, N.H., Incerti, S., Villagrasa, C., Perrot, Y., Štěpán, V., Okada, S., Moreno-Barbosa, E., and Faddegon, B., Med. Phys., 47 (11) (2020) 5919.

[51] Meylan, S., Incerti, S., Karamitros, M., Tang, N., Bueno, M., Clairand, I., and Villagrasa, C., Sci. Rep., 7 (1) (2017) 11923.

[52] Chatzipapas, K.P. et al., Precis. Radiat. Oncol., 7 (2023) 4.

[53] Hilbert, D. and Hilbert, D., "Über die stetige Abbildung einer Linie auf ein Flächenstück", In: "Dritter Band: Analysis·Grundlagen der Mathematik·Physik Verschiedenes", (Nebst Einer Lebensgeschichte, 1-2, 1935)

[54] Sakata, D. et al., Phys. Med., 62 (2019) 152.

[55] Shin, W.G., Sakata, D., Lampe, N., Belov, O., Tran, N.H., Petrovic, I., Ristic-Fira, A., Dordevic, M., Bernal, M.A., Bordage, M.C., Francis, Z., Kyriakou, I., Perrot, Y., Sasaki, T., Villagrasa, C., Guatelli, S., Breton, V., Emfietzoglou, D., and Incerti, S., Cancers, 13 (19) (2021) 4940.

[56] Cirrone, G.A.P. et al., Prog. Nucl. Sci. Technol., 2 (2011) 207.

[57] Tramontana, A. et al., Proc. 6th Int. Particle Accel. Conf. (IPAC'15), Richmond, VA, USA, May 3-8, 2015 (pp. 2515-2518). JACOW, Geneva, Switzerland.

[58] Tommasino, F. et al., Phys. Med., 58 (2019) 99.

[59] Nikjoo, H., O'Neill, P., Goodhead, D.T., and Terrissol, M., Int. J. Radiat. Biol., 71 (5) (1997) 467.

[60] Mortazavi, S.M.J., Rafiepour, P., Mortazavi, S.A.R., Razavi Toosi, S.M.T., Shomal, P.R., and Sihver, L., Med. Phys., 34 (1) (2024) 166.

[61] Francis, Z., Villagrasa, C., and Clairand, I., Com. Methods Programs Biomed., 101 (3) (2011) 265.

[62] Bertolet, A., Ramos-Méndez, J., McNamara, A., Yoo, D., Ingram, S., Henthorn, N., Warmenhoven, J.W., Faddegon, B., Merchant, M., McMahon, S.J., Paganetti, H., and Schuemann, J., Radiat. Res., 198 (3) (2022) 207.

[63] Lampe, N. et al., Phys. Med., 48 (2018) 135.

[64] Sakata, D., Belov, O., Bordage, M.C., Emfietzoglou, D., Guatelli, S., Inaniwa, T., Ivanchenko, V., Karamitros, M., Kyriakou, I., Lampe, N., Petrovic, I., Ristic-Fira, A., Shin, W.G., and Incerti, S., Sci. Rep., 10 (1) (2020) 20788.

[65] Sakata, D. et al., Phys. Med., 105 (2023) 102508.

[66] Stewart, R.D., Radiat. Res., 156 (4) (2001) 365.

[67] Elsässer, T., Weyrather, W.K., Friedrich, T., Durante, M., Iancu, G., Krämer, M., Kragl, G., Brons, S., Winter, M., Weber, K.J., and Scholz, M., Int. J. Radiat. Oncol. Biol. Phys., 78 (4) (2010) 1177.

[68] Cirrone, G.A.P., Manti, L., Margarone, D., Petringa, G., Giuffrida, L., Minopoli, A., Picciotto, A., Russo, G., Cammarata, F., Pisciotta, P., Perozziello, F.M., Romano, F., Marchese, V., Milluzzo, G., Scuderi, V., Cuttone, G., and Korn, G., Sci. Rep., 8 (1) (2018) 1141.

[69] Shahmohammadi Beni, M., Islam, M.R., Kim, K.M., Krstic, D., Nikezic, D., Yu, K.N., and Watabe, H., Sci. Rep., 12 (1) (2022) 18098.

[70] McKinnon, S., Guatelli, S., Incerti, S., Ivanchenko, V., Konstantinov, K., Corde, S., Lerch, M., Tehei, M., and Rosenfeld, A., Phys. Med., 32 (12) (2016) 1584.

[71] Ahmad, R., Royle, G., Lourenço, A., Schwarz, M., Fracchiolla, F., and Ricketts, K., Phys. Med. Biol., 61 (12) (2016) 4537.

[72] Rashid, R.A. et al., OpenNano, 4, (2019) 100027.

[73] Zwiehoff, S., Johny, J., Behrends, C., Landmann, A., Mentzel, F., Bäumer, C., Kröninger, K., Rehbock, C., Timmermann, B., and Barcikowski, S., Small, 18 (9) (2022) e2106383.

[74] Ganjeh, Z.A., Eslami-Kalantari, M., Loushab, M.E., and Mowlavi, A.A., Radiat. Phys. Chem., 179 (2021) 109249.

[75] Roots, R., Holley, W., Chatterjee, A., Irizarry, M., and Kraft, G., Int. J. Radiat. Biol., 58 (1) (1990) 55.

[76] Hirayama, R., Ito, A., Tomita, M., Tsukada, T., Yatagai, F., Noguchi, M., Matsumoto, Y., Kase, Y., Ando, K., Okayasu, R., and Furusawa, Y., Radiat. Res., 171 (2) (2009) 212.

[77] Ito, A., Nakano, H., Kusano, Y., Hirayama, R., Furusawa, Y., Murayama, C., Mori, T., Katsumura, Y., and Shinohara, K., Radiat. Res., 165 (6) (2006) 703.

[78] Chattaraj, A. and Selvam, T.P., Biomed. Phys. Eng. Express, 10 (4) (2024) 045059.

[79] Rafiepour, P., Sina, S., Amoli, Z.A., Shekarforoush, S.S., Farajzadeh, E., and Mortazavi, S.M.J., Phys. Eng. Sci. Med., 47 (3) (2024) 1015.

[80] Jeynes, J.C., Merchant, M.J., Spindler, A., Wera, A.C., and Kirkby, K.J., Phys. Med. Biol., 59 (21) (2014) 6431.

[81] Li, S., Penninckx, S., Karmani, L., Heuskin, A.C., Watillon, K., Marega, R., Zola, J., Corvaglia, V., Genard, G., Gallez, B., Feron, O., Martinive, P., Bonifazi, D., Michiels, C., and Lucas, S., Nanotechnology, 27 (45) (2016) 455101.